Solar Phys (2012) 281:793–813
DOI 10.1007/s11207-012-0101-y

Relation Between Coronal Hole Areas on the Sun and the Solar Wind Parameters at 1 AU

T. Rotter · A.M. Veronig · M. Temmer · B. Vršnak

Received: 12 March 2012 / Accepted: 8 August 2012 / Published online: 7 September 2012

Abstract We analyze the relationship between the coronal hole (CH) characteristics on the Sun (area, position, and intensity levels) and the corresponding solar wind parameters (solar wind speed v, proton temperature T, proton density n, and magnetic field strength B) measured *in situ* at 1 AU with a 6-h time resolution. We developed a histogram-based intensity thresholding method to obtain fractional CH areas from SOHO/EIT 195 Å images. The algorithm was applied to 6-h cadence EIT 195 Å images for the year 2005, which were characterized by a low solar activity. In calculating well-defined peaks of the solar wind parameters corresponding to the peaks in CH area, we found that the solar wind speed v shows a high correlation with correlation coefficient cc $= 0.78$, medium correlation for T and B with cc $= 0.41$ and cc $= 0.41$. No significant correlation was found with the proton density n. Applying an intensity-weighted CH area did not improve the relations, since the size and the mean intensity of the CH areas are not independent parameters but strongly correlated (cc $= -0.72$). Comparison of the fractional CH areas derived from GOES/SXI and SOHO/EIT and the related solar wind predictions shows no systematic differences (cc $=$ 0.79).

Keywords Coronal holes · Solar wind

T. Rotter (✉) · A.M. Veronig · M. Temmer
Kanzelhöhe Observatory-IGAM, Institute of Physics, University of Graz, Universitätsplatz 5, 8010 Graz, Austria
e-mail: thomas.rotter@uni-graz.at

A.M. Veronig
e-mail: asv@igam.uni-graz.at

B. Vršnak
Hvar Observatory, Faculty of Geodesy, Zagreb, Croatia
e-mail: bvrsnak@geodet.geof.hr

1. Introduction

Coronal holes (CHs) are low density regions in the solar corona visible as dark areas due to their lower temperature and density compared to the surrounding coronal plasma (Munro and Withbroe, 1972; for a review see Cranmer, 2009). Coronal holes are most easily observed in space-based X-ray (Wilcox, 1968; Altschuler, Trotter, and Orrall, 1972; Hundhausen, 1972) and EUV images (Newkirk, 1967; Tousey, Sandlin, and Purcell, 1968; Del Zanna and Bromage, 1999). They coincide with rapidly expanding open magnetic fields and are the source region of the high speed solar wind streams (HSSs) that play an important role in geomagnetic storm activity (Krieger, Timothy, and Roelof, 1973; Neupert and Pizzo, 1974; Tsurutani *et al.*, 1995; Gosling and Pizzo, 1999). In the past, coronal holes have been identified visually and manually tracked by experienced observers. More recently, there have been a few attempts to automate the process for the identification and detection of coronal holes using different techniques, such as perimeter tracing (Kirk *et al.*, 2009), intensity thresholding (Krista and Gallagher, 2009; de Toma, 2011), fuzzy clustering (Barra *et al.*, 2009), multichannel segmentation (Delouille, Barra, and Hochedez, 2007), and edge-based segmentation (Scholl and Habbal, 2008).

Besides CMEs and flares, HSSs are the most dominant factor causing geomagnetic storms. One way to predict the physical parameters of the solar wind is by using synoptic solar magnetic field maps as input for heliospheric magnetohydrodynamic (MHD) codes like *e.g.* ENLIL (a numerical model simulating the ambient corotating solar wind; Odstrcil and Pizzo, 2009) or empirical/numerical hybrid models, *e.g.* the Hybrid Heliospheric Modeling System (HHMS; Detman *et al.*, 2006). However, since CHs are long-lived structures on the Sun, which may persist for several solar rotations, the HSS characteristics at 1 AU should also be predictable from the CH observations. Several teams already have investigated the statistical relationship between coronal holes and studied how their size and location determine the solar wind parameters and geomagnetic effects measured at 1 AU (Nolte *et al.*, 1976; Robbins, Henney, and Harvey, 2006; Vršnak, Temmer, and Veronig, 2007a, 2007b; Luo *et al.*, 2008; Abramenko, Yurchyshyn, and Watanabe, 2009; Obridko *et al.*, 2009; Verbanac *et al.*, 2011).

Using the unprecedented continuous observations by the *Solar and Heliospheric Observatory* (SOHO) Extreme ultraviolet Imaging Telescope (EIT; Delaboudinière *et al.*, 1995) since 1997, we have now for the first time the chance to study the behavior of coronal hole areas and the related solar wind parameters over a full solar cycle (cycle 23). In the present paper we focus on the declining phase of solar cycle 23, year 2005, to test the ability of EUV observations in extracting CH areas, and in predicting the solar wind characteristics at 1 AU during conditions of low CME activity. We will compare our results for the year 2005 using EIT 195 Å images to extract the CH fractional areas and to study their relation with the solar wind characteristics near the Earth with previous work using solar X-ray images (Reeves and Parkinson, 1970; Krieger, Timothy, and Roelof, 1973; Vaiana, 1976; Vršnak, Temmer, and Veronig, 2007a; Obridko *et al.*, 2009; Verbanac *et al.*, 2011), where coronal holes are in general better observed due to the broader response function. In a follow-up study, the derived methods will be used to study the coronal hole evolution and related solar wind characteristics over the full solar cycle 23 in SOHO/EIT observations. In addition, the CH extraction algorithm presented in this paper will also be applied to almost real-time EUV imagery by the AIA instrument (Lemen *et al.*, 2012) onboard the *Solar Dynamics Observatory* (SDO) to predict the solar wind characteristics (in particular solar wind speed) at 1 AU up to 3 days in advance.

In Section 2 we describe the data used for our study. Section 3 describes the algorithm for segmenting coronal hole areas in SOHO/EIT 195 Å images. The results will be presented

in Section 4. In Section 4.1, we establish the relations between the CH areas derived in EIT 195 Å images and the solar wind characteristics at 1 AU. In Section 4.2 we test if the additional consideration of the "darkness" of the CHs improve the capability of solar wind predictions. In Section 4.3, we compare the results from EIT 195 Å with those obtained from the Solar X-ray Imager (SXI; Hill *et al.*, 2005; Pizzo *et al.*, 2005) onboard the GOES-12 spacecraft. The results are discussed in Section 5.

2. Data

Our analysis is based on the following data sets:

- fractional area A of coronal holes derived via histogram-based thresholding methods applied to SOHO/EIT 195 Å and GOES SXI images;
- solar wind parameters: speed v, temperature T, density n, and magnetic field strength B measured *in situ* at L1.

For the extraction of coronal hole areas we use the 1024×1024 fits data cubes provided by EIT onboard the SOHO satellite with a cadence of ≈ 12 min in the 195 Å band (dominated by emission of the Fe XII ion, $T \approx 1.5$ MK). For our purposes we utilize images with a cadence of approximately 6 h, taken at 1, 7, 13, and 19 UT. The EIT images are reduced with the EIT software routines provided within SolarSoft. In addition, solar CH fractional areas were also determined by soft X-ray images with a 6-h interval, acquired by SXI.

We utilize the solar wind data measured *in situ* at 1 AU by Solar Wind Electron Proton and Alpha Monitor (SWEPAM; McComas *et al.*, 1998) and the magnetometer instrument (MAG; Smith *et al.*, 1998) on board the *Advanced Composition Explorer* (ACE; Stone *et al.*, 1998). The hourly averaged level-2 ACE data, available at http://www.srl.caltech.edu/ACE/ASC/level2/, were time-averaged to a 6-h data resolution.

In this paper we focus on the year 2005, characterized by a very low CME activity. Due to data gaps in the EIT archive (DOY 70 – 91, DOY 157 – 176, DOY 244 – 268, and DOY 336 – 353) it was not possible to use a coherent data set for the full year 2005. In total, we processed a set of 1011 EIT 195 Å images.

3. Methods of Analysis

Our goal is to fully automate the process of identification and extraction of coronal hole regions in SOHO/EIT 195 Å images. The algorithm performs the following main steps:

i) it automatically selects images for our purposes,
ii) it detects and defines the boundaries of CHs via intensity histograms to obtain binary maps, and
iii) it uses morphological methods on the created binary maps in order to improve the detection of CH areas.

In step 1, we refine the pool of the available SOHO/EIT 195 Å images to a 6-h cadence, *i.e.* four images per day recorded at roughly 1, 7, 13, and 19 UT. We reject images with corrupted pixel blocks and images where intense flares and CMEs cause disturbances or

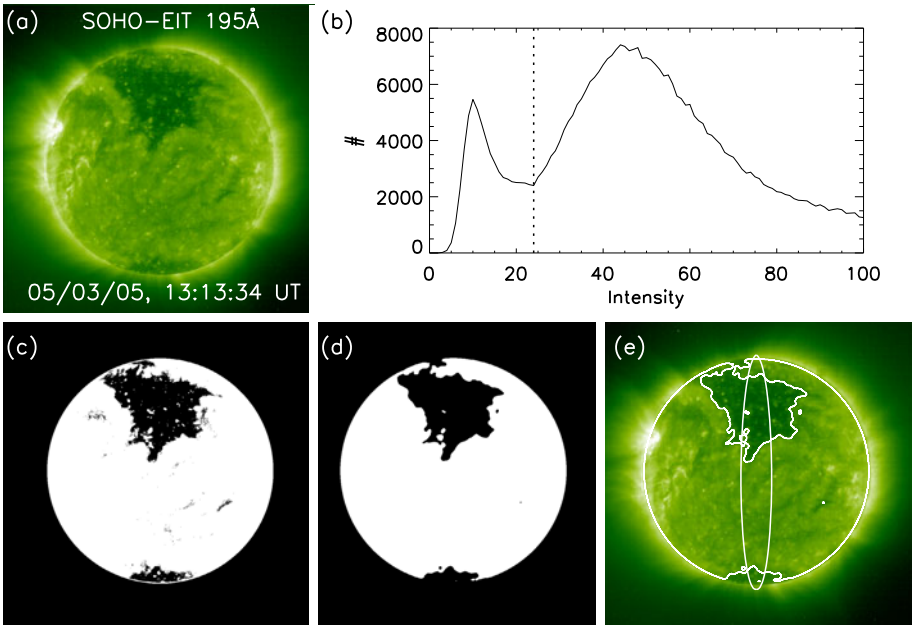

Figure 1 (a) Calibrated EIT 195 Å image recorded on 3 March 2005 at 13:13:34 UT. (b) Histogram of the solar disc intensities. The vertical dashed line indicates the chosen CH threshold. (c) Resulting binary map after application of the determined CH threshold. (d) Fully processed binary map, after application of erosion and dilation. (e) CH binary map overlaid on the original EIT image. The meridional slice considered, $[-7.5°, 7.5°]$, is also drawn.

hot pixels on the image. Selecting suitable images for the further analysis happens fully automatically by the algorithm, but it was also manually cross-checked.

In step 2 we make use of the simple but powerful thresholding segmentation technique. Via thresholding one can easily determine certain regions of interest (ROI) in an image and create binary maps for further investigation. CHs are characterized by their low intensities compared to the surrounding corona, and can thus be well identified via techniques based on thresholding (Krista and Gallagher, 2009; de Toma, 2011). A key parameter in the thresholding process is the choice of suitable thresholds. One mathematical approach to achieve suitable thresholds is to study the distribution of the intensity of image pixels.

Figure 1 illustrates how the algorithm works. Panel (a) shows the original calibrated EIT 195 Å image recorded on 5 March 2005 at 13:13:34 UT. A large CH at the northern hemisphere and a smaller, fainter (in contrast) CH located at the solar southpole are clearly visible. Panel (b) shows the histogram of the solar disk of the original EIT image. All pixels above the solar limb are excluded. The x-axis indicates the intensity values given in digital numbers (DNs) and the y-axis shows the corresponding number of pixels within the chosen intensity bins. The histogram shows a bimodial distribution, *i.e.* two peaks and a valley in-between. The first peak in the distribution (at lower intensities) represents CH pixels. The minimum value between the two peaks is taken as an upper threshold level for CHs. Pixels with lower intensities are marked as 0 and those with higher intensities are marked as 1, resulting in a binary map as shown in panel (c). Experience shows that CH intensity pixel values in the EIT 195 Å images lie at 25 ± 5 DNs (stable threshold-levels in the detection of CHs in EUV images were also mentioned in the study of Krista and Gallagher, 2009).

In Figure 1(b) the upper CH intensity threshold obtained is 24. Consequentially all intensity values below 24 are set to 0 and all values above 24 are set to 1. If the algorithm is not able to detect a well-defined minimum in the distribution (which is the case if the total CH area is small), the threshold is set to 28 DN.

For the automatized detection of CH pixels at higher latitudes and longitudes we added a threshold multiplier, since CHs close to the limb appear less dark, due to the optically thin emission from neighboring coronal structures. This adaptive thresholding algorithm varies threshold values for different location by using a multiplier, which steadily increases from 1.0 up to 1.4 from 60° up to 90° latitude and/or longitude. With this refinement, polar CHs are also well detected although they have a smaller contrast.

In step 3, after automatically finding a suitable threshold value to create the binary maps, we process the binary maps by using morphological methods. Erosion and Dilation are two basic operators in the area of mathematical morphology that are typically applied to binary maps, and have previously been applied for the detection of CHs (Henney and Harvey, 2005). The basic effects of the operators on binary maps are to erode (or shrink) the boundaries of regions, removing all small anomalies (Erosion) and to gradually expand the boundaries of regions to fill small holes in-between (Dilation). In order to apply these operators we had to find a proper structuring element (a.k.a. kernel) that determines the precise effect of the erosion or dilation. In our studies we superimpose a box of 16×16 pixels on top of the input image. The kernel basically works like a median filter, exchanging the 0 and 1 values of the binary map under given circumstances. Figure 1(d) shows a fully processed binary map. In comparison to the starting binary map in Figure 1(c), small structures have been removed and small gaps in CH regions have been filled up.

In Figure 1(e) the fully processed binary map is overlaid on the original calibrated EIT map displaying the contours of the detected CH regions. White lines surrounding the outer edge of the solar disk are mere artifacts caused by the algorithm during the transformation process creating binary maps; they have no effect on any further calculations. The meridional slice embracing the central meridian at $\pm 7.5°$ in longitude is also outlined. In this study we used a $\pm 7.5°$-sized slice centered at the solar meridian for our calculations. All pixels identified as CH pixels inside this meridional slice are summed up and divided by the total number of pixels in the slice. This fractional CH area, A, is used in the following analysis. The total longitudinal extent of 15° covered by our slice corresponds roughly to the average solar rotation during one day. Since we calculated the CH fractional areas from EIT images with a 6-h cadence, subsequent data points of the derived CH areas are not independent but a correlated average of about four subsequent data points. This acts like a smoothing function on the CH area time series. In principle, one could choose smaller slices in which the instant CH areas are derived but this comes with higher statistical fluctuations due to the small area of the solar disk considered. In Vršnak, Temmer, and Veronig (2007a) it was shown that choosing a slice centered on the eastern hemisphere one can enhance the lead time for the forecasting, since the related coronal hole area located is further away from being magnetically connected to the Earth than one centered on the meridian or the western hemisphere. On the other hand, the CHs evolve during this time, which degrades the correlation between CH area and solar wind parameters at 1 AU. Thus, it was concluded that the central meridional slice provides a good compromise between predictive lead time (which may be up to 4 days for the solar wind speed parameter) and instant coronal hole property.

4. Results

During the year 2005, several long-lived equatorial CHs were present on the Sun, resulting in periodically occurring peaks in the CH fractional areas A (Figure 2(a)). These peaks in the CH fractional areas are also reflected in peaks in solar wind data observed at 1 AU (though with a delay of up to 4 days; see Vršnak, Temmer, and Veronig, 2007a), *i.e.* speed, temperature, density, and magnetic field strength (Figures 2(b) – (e)).

In the following sections we study the correlations between CH areas and solar wind parameters at 1 AU. In order to assess the significance of the correlations and to obtain a robust estimate of the correlation coefficients, we applied bootstrapping (Wall and Jenkins, 2003). The bootstrap method works in the following simple way: Out of the sample of N events, we draw repeatedly N events at random, and compute the correlation coefficient for each of these realizations. This procedure is repeated 1000 times, and the average value of the distribution of the correlations coefficients and its standard variation are calculated.

4.1. Comparison of EIT CH Areas and Solar Wind Parameters

In forecasting space weather effects of HSSs at the Earth, two parameters are of major interest: the arrival time and the predicted peak values – when does the solar wind hit the detectors and at what speed? In order to quantify the arrival times of the characteristic solar wind disturbances a cross-correlation method was applied on CH fractional areas A with the solar wind speed v, temperature T, density n, and total magnetic field strength B. In former studies (*e.g.* Vršnak, Temmer, and Veronig, 2007a) the period of DOY 25 – 125 was preferably considered due to very low CME activity. Due to data gaps in the EIT archive, we used different time windows (DOY 25 – 75, 124 – 146, 266 – 295, and 307 – 336) in our study, all indicating similar trends. Figure 3 shows the A–v, A–T, A–n and A–B cross-correlations in the period of DOY 25 – 75 with a time resolution of 6 h. The cross-correlation method was applied for a time lag of ± 20 days and the black vertical line indicates the derived time lag with highest correlation.

Highest correlation coefficients were found for the A–v relationship at a lag of 3.5 days, A–T at 2.75 days, A–n at 0.75, and A–B at 1.25 days. This is similar to the results of Vršnak, Temmer, and Veronig (2007a) and Verbanac *et al.* (2011). Surprisingly, the solar wind density and magnetic field delays are shorter than the expected solar wind transit time of 2 – 3 days. In order to explain the different arrival times characterized by various solar wind parameters, one has to take interactions at the corotating interaction regions (CIRs) or HSS and their physical impact on the Parker spiral into account. The fast solar wind streams originating from the CH interacts with the slow solar wind and causes CIR-compression regions at the frontal side of the HSS (Gosling, 1996). Due to the large longitudinal extent of CHs, the leading edge of the HSS may have passed the central meridian up to 1 – 3 days in advance compared to the CH central region (see also Vršnak, Temmer, and Veronig, 2007a; Verbanac *et al.*, 2011). The frozen-in magnetic field gets compressed and therefore also shows a small delay time. The enhancements in solar wind temperature and speed are not subject to compression, and thus they rise more slowly, until peaking in the center of the HSS.

After obtaining the delays of solar wind parameters compared to the fractional solar CH areas A via cross-correlation, we shift the A time series with the corresponding lag and correlate the outcome with measured solar wind parameters. For instance, A is shifted by 3.5 days and correlated with the *in situ* measured solar wind speed v. Figure 4 shows the applied time-lagged scatter plots of the fractional CH area A with the corresponding

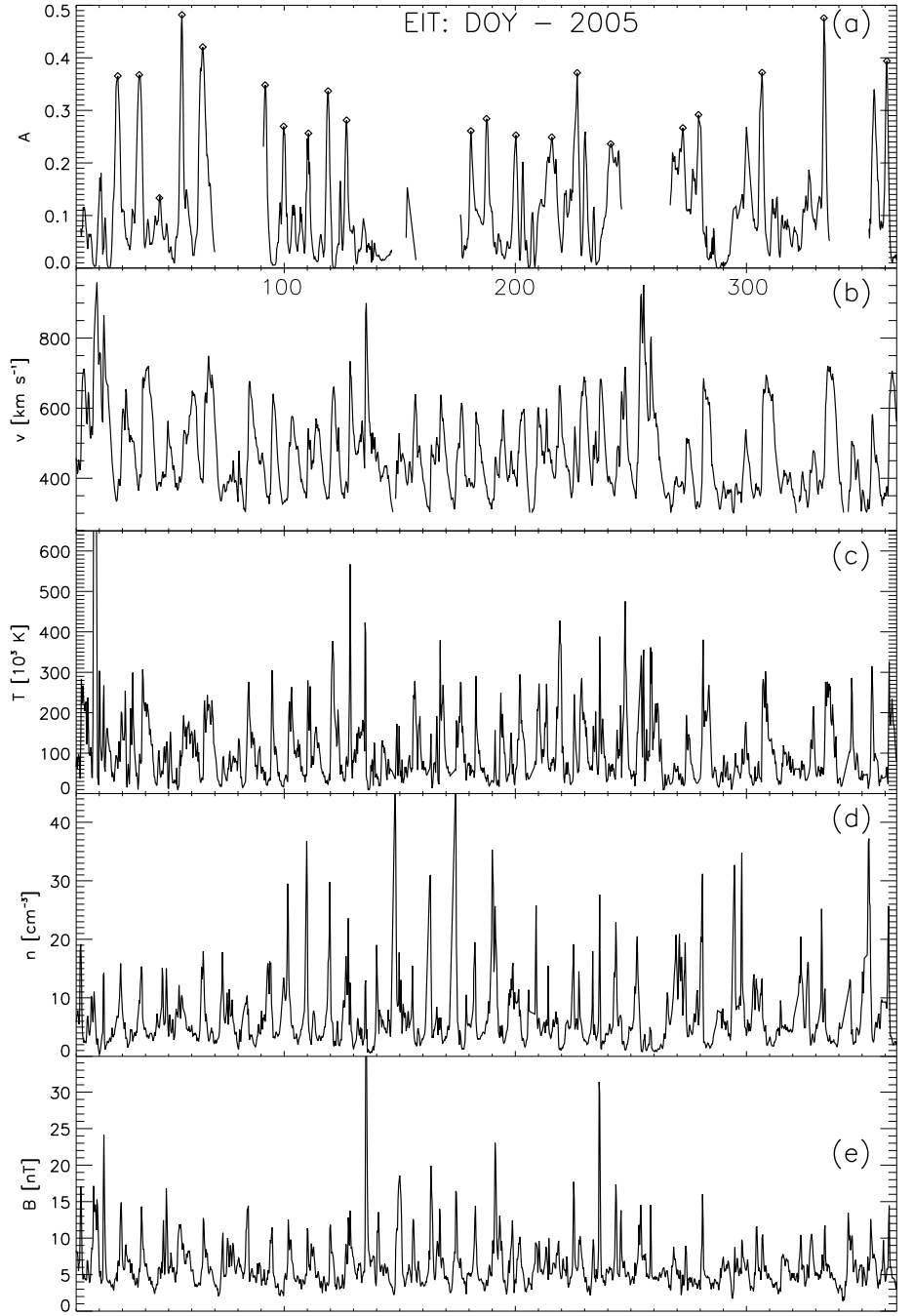

Figure 2 (a) Fractional CH area derived from EIT 195 Å images for the year 2005. Diamonds indicate peaks used in the analysis. (b) *In situ* measured solar wind speed v, (c) temperature T, (d) density n, and (e) total magnetic field strength B at 1 AU.

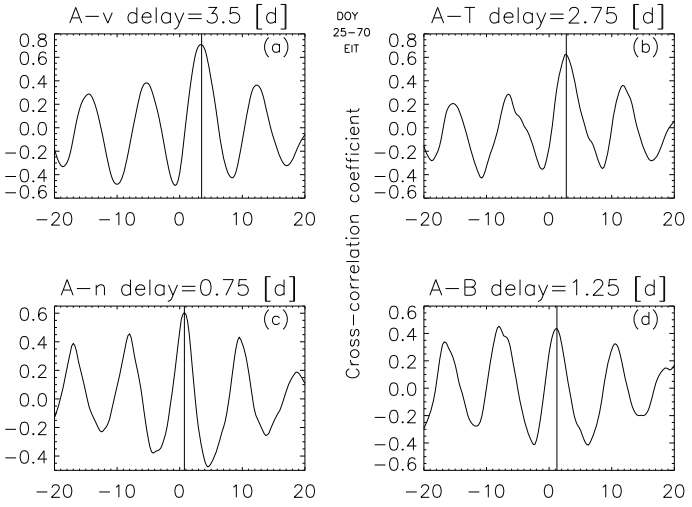

Figure 3 Cross-correlation coefficients derived from the DOY 25 – 70 6-h data of the CH fractional A obtained from EIT 195 Å images and the corresponding ACE solar wind parameters: (a) speed v, (b) proton temperature T, (c) density n, and (d) total magnetic field strength B. The cross-correlation function was calculated up to a time lag of ± 20 days. The vertical lines represent the time lags with highest correlation.

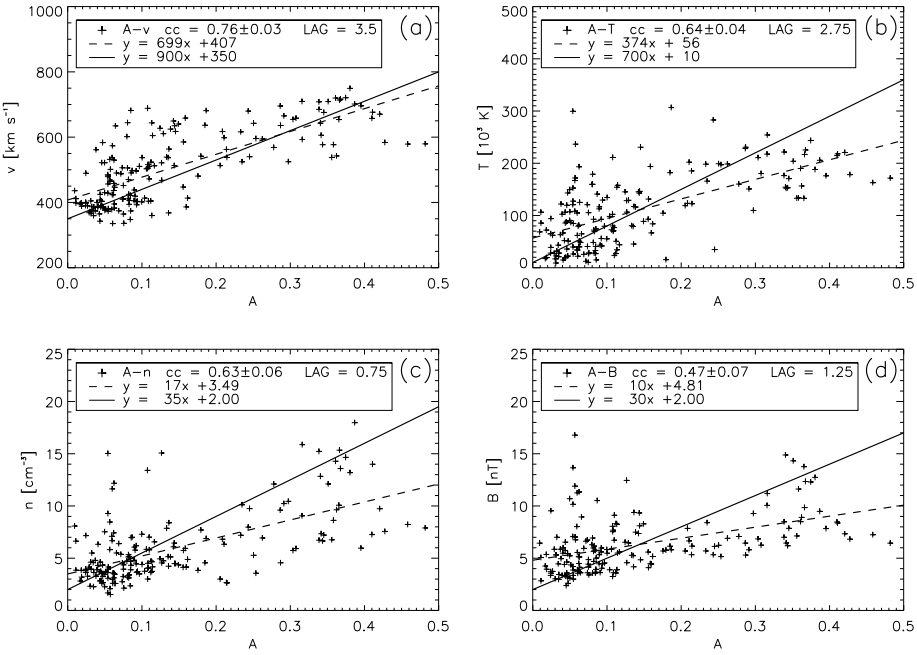

Figure 4 Correlations of the time-lagged CH fractional areas A with (a) solar wind speed v, (b) proton temperature T, (c) density n, and (d) total magnetic field strength B for the period of DOY 25 – 70. The time lag applied for the correlation and the corresponding correlation coefficients are given in insets. Dashed lines denote the regression lines and thick lines show the amplitude optimized functions.

solar wind parameters. A–v, A–T, A–n and A–B pairs give the correlation coefficients cc $= 0.76 \pm 0.03$, 0.64 ± 0.04, 0.63 ± 0.06, and 0.47 ± 0.07. The dashed line indicates the least-squares linear fits. Due to its mathematical nature it tends to underestimate and smooth out peak values, and is thus not well suited as a functional form for the forecasting procedure (see also Vršnak, Temmer, and Veronig, 2007a). The full line in Figure 4 represents an amplitude-optimized function, a linear function that delivers a forecast option:

$$f(t) = c_0 + c_1 A(t_{\text{lag}}), \tag{1}$$

where c_0 and c_1 are the substituting coefficients, and $A(t_{\text{lag}})$ is the fractional area shifted in time according to the time lags found. In the case of the solar wind speed (panel (a)), c_0 is 350 and c_1 is 900. T, n, and B were treated in the same way resulting in $c_0 = 10$, 2, 2 and $c_1 = 700$, 35, 30.

By applying Equation (1) to A for the EIT 195 Å images of the full year 2005 we derive the prediction curves for $v(t)$, $T(t)$, $n(t)$, and $B(t)$ plotted in Figure 5. The black lines represent the derived fractional CH area A (panel (a)) and the *in situ* measured solar wind speed v (Figure 5(b)), proton temperature T (Figure 5(c)), density n (Figure 5(d)), and the total magnetic field strength B (Figure 5(e)). Red lines denote the solar wind values predicted from the fractional CH areas A.

In Figure 6 we zoom in on the time window DOY 25 – 130. Figures 6(a) – (d) show the measured v, T, n, and B values (black lines) and the corresponding predicted values (red lines). One sees that the highest accuracy is provided for the solar wind speed v and the temperature T. The density n and the magnetic field strength B are less well predicted (time-wise and peak-value-wise) by the algorithm.

Figure 7 depicts the correlation between the measured and predicted peak values for 21 well-defined peaks of the solar wind parameters in the time range 25 – 365 (indicated by diamonds in Figure 2). The correlation analysis shows a high correlation for the predicted versus measured solar wind speed peaks with cc $= 0.78 \pm 0.08$. A medium correlation for the temperature T with cc $= 0.41 \pm 0.22$ and the magnetic field strength B with cc $= 0.41 \pm 0.16$ was found. For the density n no significant correlation coefficient cc $= 0.18 \pm 0.19$ was obtained. In this respect, it is important to bear in mind that for the prediction of geomagnetic activity v and B are most relevant parameters.

4.2. Comparison of Intensity-Weighted EIT CH Areas and Solar Wind Parameters

CHs are regions that are less dense and less hot than the ambient corona (Munro and Withbroe, 1972), and thus appear as dark regions in X-ray and EUV wavelengths (Reeves and Parkinson, 1970; Vaiana, 1976). Since it was reported that the CH brightness (contrast) correlates with the characteristics of the solar wind at 1 AU, especially v (see Veselovsky *et al.*, 2006; Robbins, Henney, and Harvey, 2006), we analyzed if EIT fractional CH areas with intensity weighting would increase the forecasting capabilities. To this aim, we weighted the fractional CH areas by the inverse of the mean intensity of the CH pixels.

Figure 8 shows the derived intensity-weighted fractional CH areas A_{w} (bottom) compared to the unweighted areas A (top panel) for the full year 2005. In general, the A and A_{w} peaks show a similar behavior. We derived the same time lags for A_{w} as we did for A and correlate the outcome with measured solar wind parameters (Figure 9). A_{w} and v correlate with cc $= 0.74 \pm 0.03$, A_{w} and T with cc $= 0.64 \pm 0.04$, A_{w} and n with cc $= 0.63 \pm 0.06$, and A_{w} and B with cc $= 0.48 \pm 0.07$. All correlations show minor differences (< 0.03) in comparison with the correlations of A with solar wind parameters (see also Figure 7). We compare the outcome delivered by the forecasts with the original and the intensity-weighted

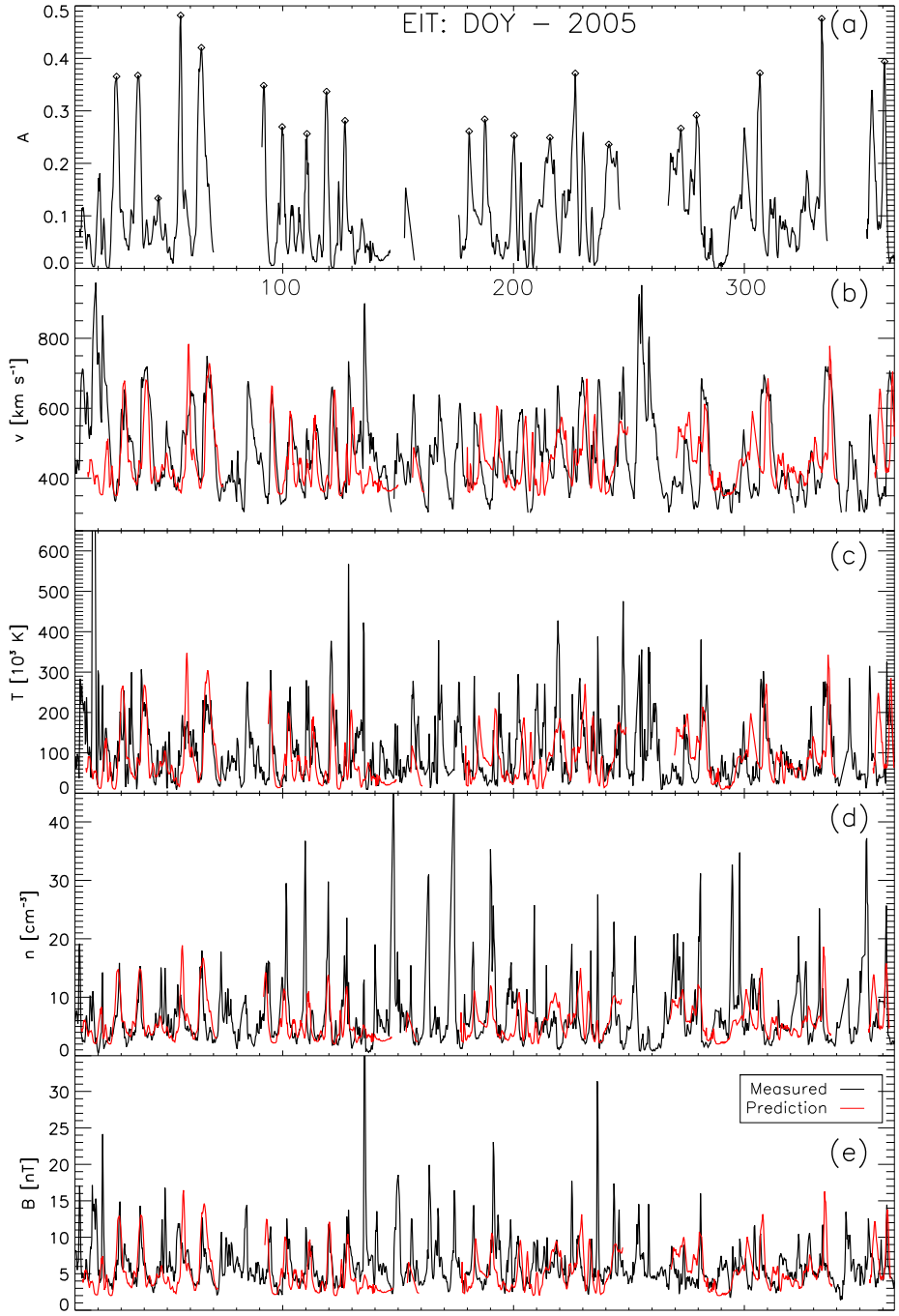

Figure 5 (a) Fractional CH area A, and the *in situ* measured (b) solar wind speed v, (c) proton temperature T, (d) density n, and (e) total magnetic field strength B at 1 AU for the year 2005. Black lines indicate the data measured. Red lines depict forecast values.

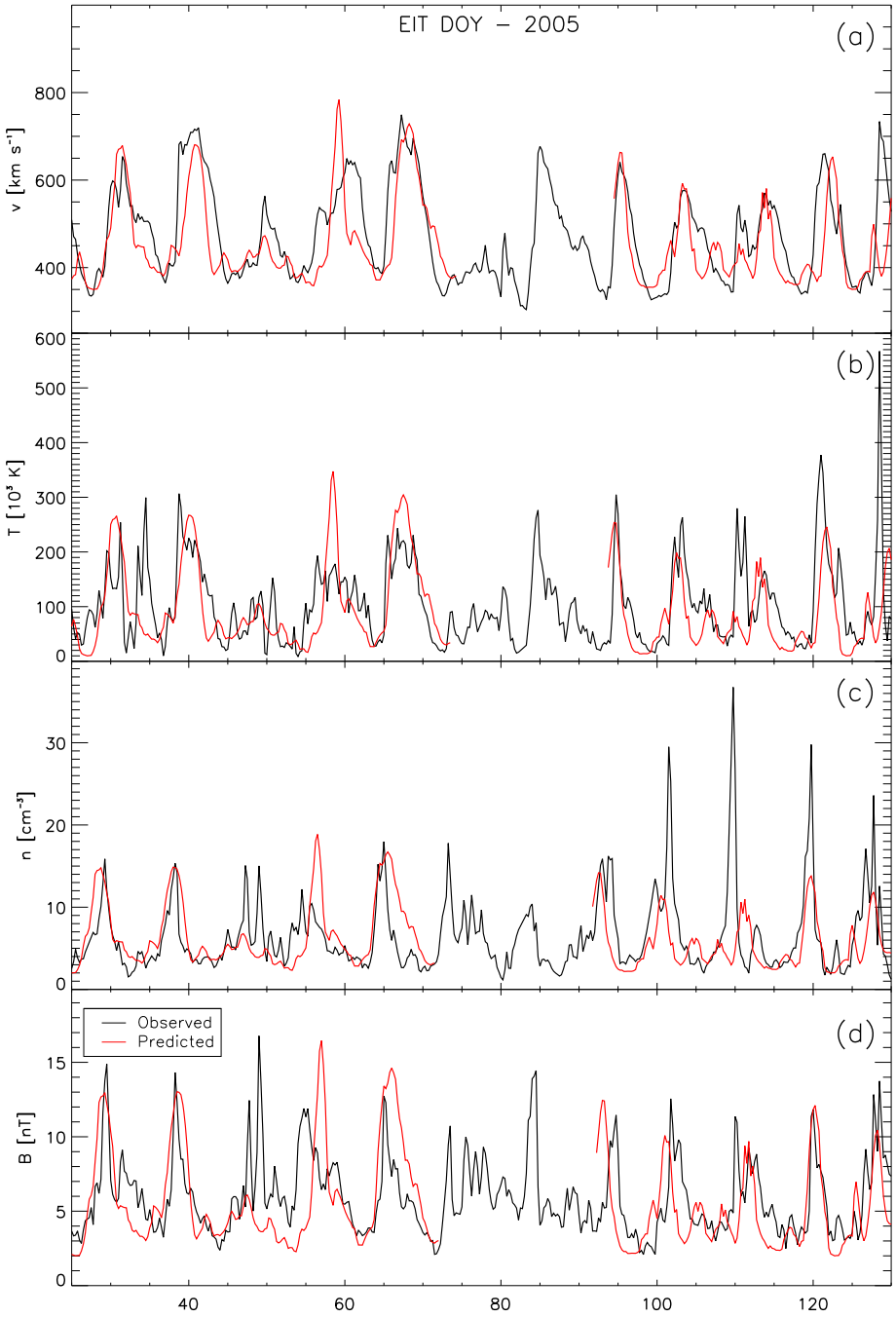

Figure 6 Same as Figure 5, but zoomed in for the period DOY 25 – 130.

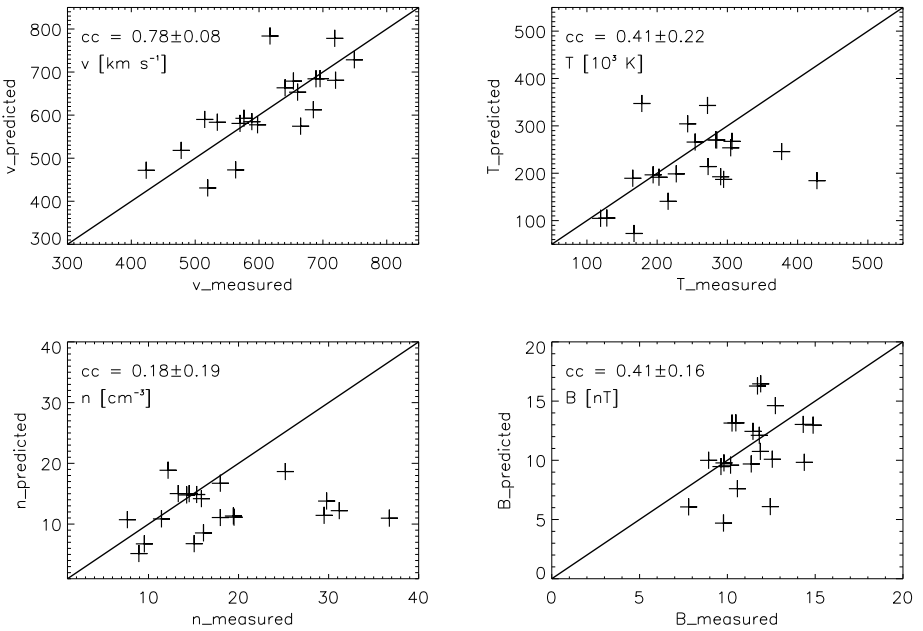

Figure 7 Comparison of 21 peaks in the fractional CH areas A (indicated in Figure 5(a)) and the corresponding solar wind parameters in the time range of DOY 25 – 365, 2005: solar wind speed v, proton temperature T, density n, and total magnetic field strength B. The related correlation coefficients are indicated in the insets. The one-to-one correspondence is plotted as a black line.

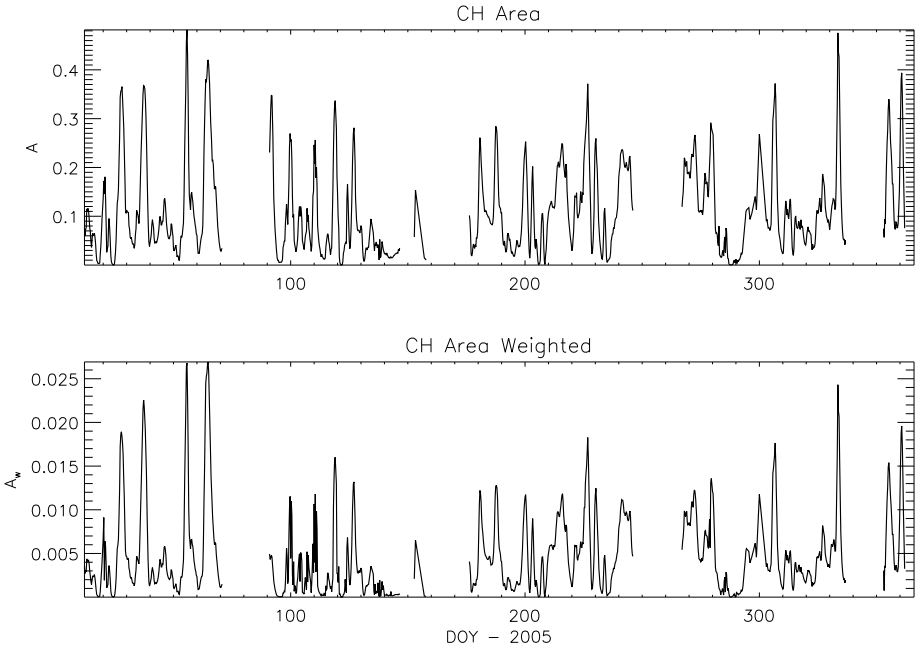

Figure 8 Top: Fractional CH areas. Bottom: Intensity-weighted fractional CH areas for the year 2005.

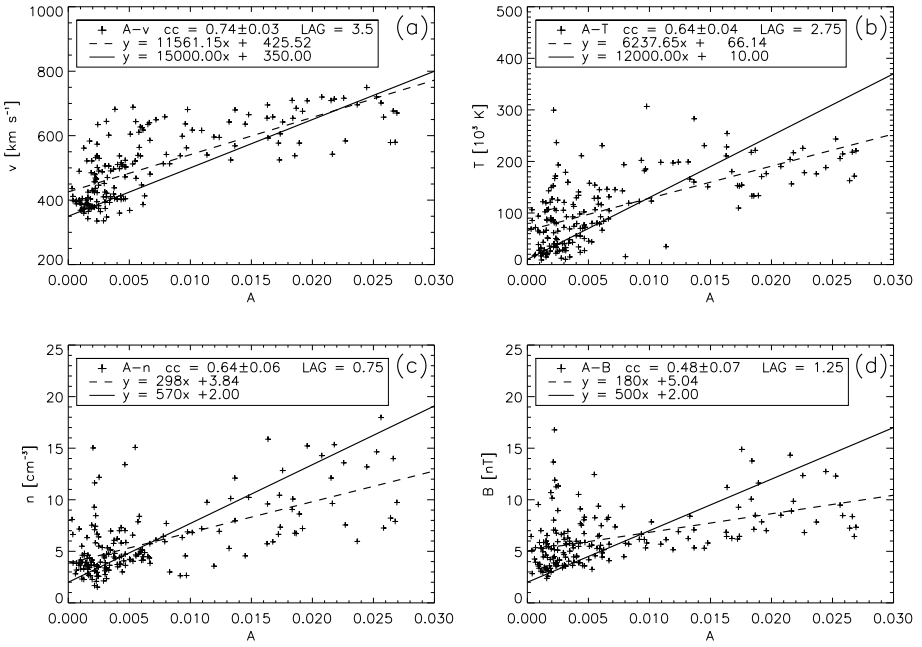

Figure 9 Correlation of the time-lagged intensity-weighted fractional CH areas with (a) solar wind speed v, (b) proton temperature T, (c) density n, and (d) total magnetic field strength B for the period of DOY 25 – 70. The time lag applied for the correlation and the corresponding correlation coefficients are given in insets. Dashed lines denote the regression lines, and thick lines show the amplitude-optimized functions.

CH areas for the time range DOY 25 – 130. Figure 10 shows the differences between the *in situ* measured values (black lines), the predictions based on the CH fractional areas A (red lines), and the predictions based on intensity-weighted CH fractional areas A_w (green lines) for v, T, n, and B. Figure 11 shows the scatter plot for the 21 selected CH area peaks with measured solar wind parameters as in Figure 7 but using the intensity-weighted areas instead. A_w and v correlate with 0.77 ± 0.11, A_w and T with 0.41 ± 0.22, A_w and n with 0.18 ± 0.17, and A_w and B with 0.40 ± 0.15. The intensity-weighted areas A_w with v, T, n, and B show correlation coefficients slightly similar to A (cc $= 0.78 \pm 0.08$, 0.41 ± 0.22, 0.18 ± 0.19, and 0.41 ± 16).

Figure 12 shows the scatter plot of the derived fractional CH areas and the mean intensity of those areas giving a correlation coefficient of -0.72 ± 0.04. This implies that the size and mean intensity of the CH areas are closely correlated and not independent parameters. The larger the CH area the darker (in contrast) it becomes. This may explain why weighting the CH area by its mean intensity does not improve the forecasts, as the intensity does not provide additional independent information.

4.3. Comparison of CH Areas Obtained from EIT and SXI

In a series of papers (Vršnak, Temmer, and Veronig, 2007a; Temmer, Vršnak, and Veronig, 2007; Verbanac *et al.*, 2011), it was established that the solar wind characteristics at 1 AU can be well predicted from the fractional CH areas determined from SXR images. In order to test if CHs determined in EUV images provide similar results, we compare the CH areas

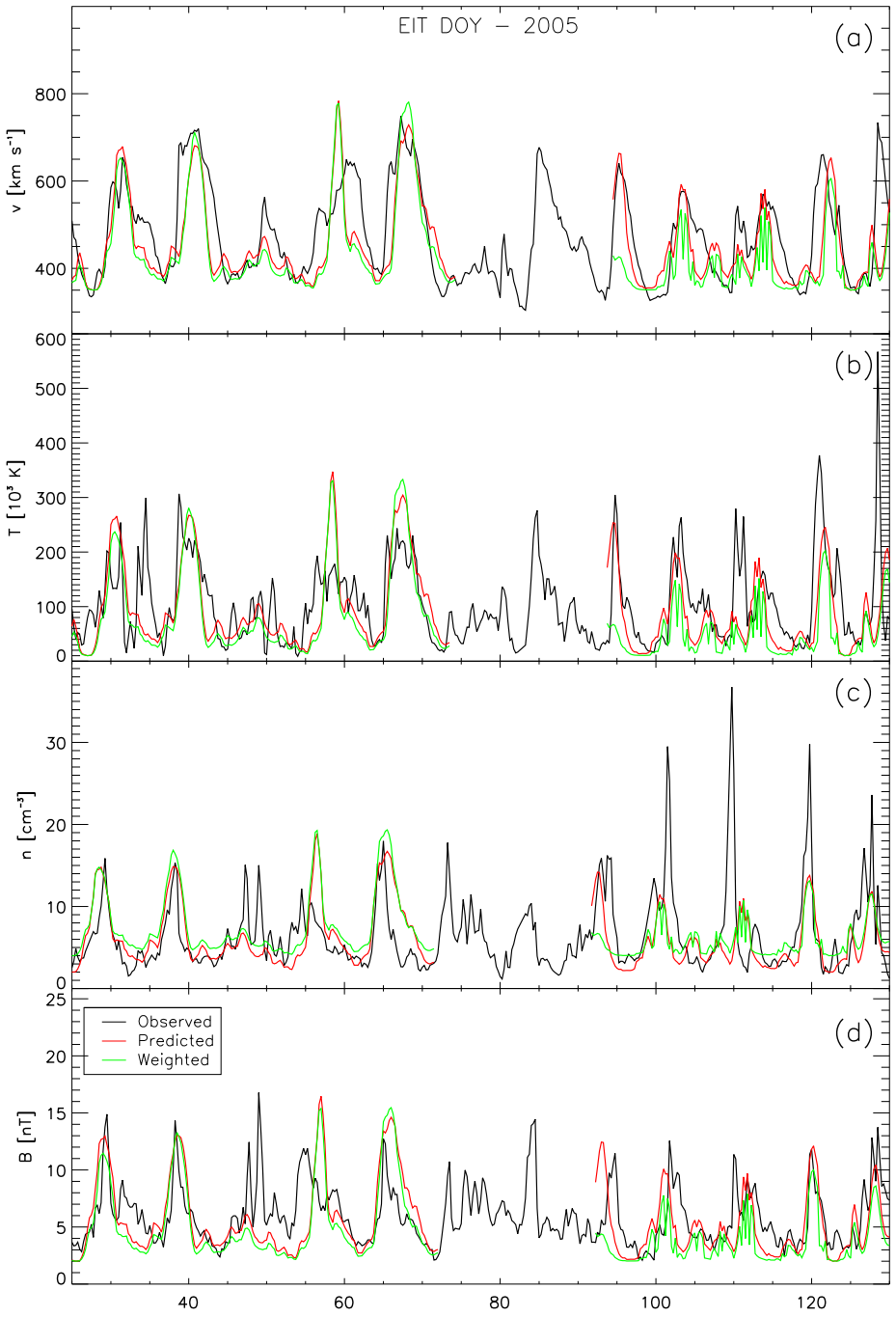

Figure 10 Comparison of *in situ* measured solar wind parameters (black lines), predictions based on CH fractional areas A (red lines), and predictions based on intensity-weighted CH areas A_{w} (green lines). From top to bottom: solar wind speed v, temperature T, density n, and total magnetic field strength B for DOY 25 – 130 of 2005.

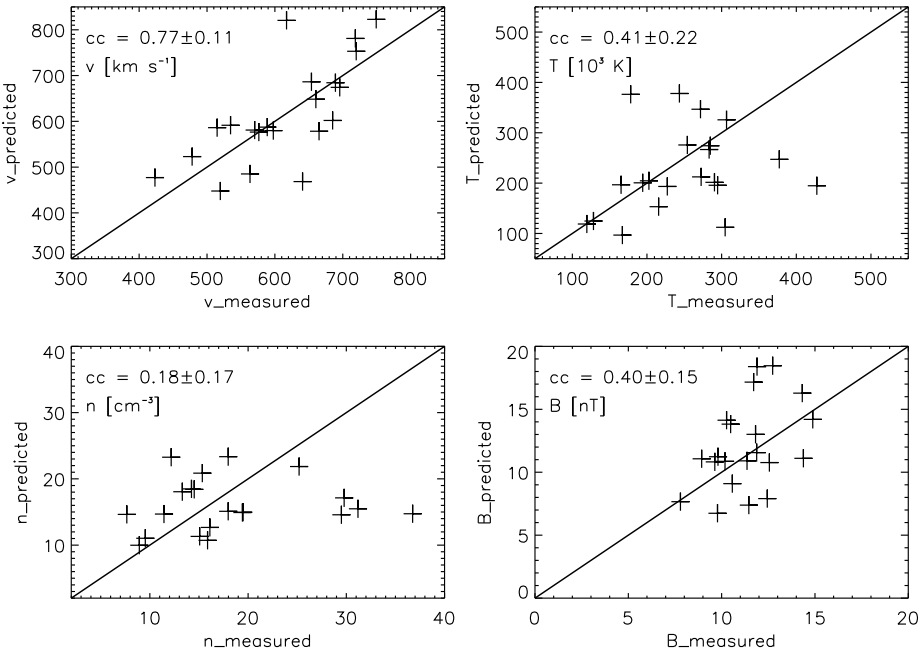

Figure 11 Same as Figure 7, but using intensity-weighted CH areas.

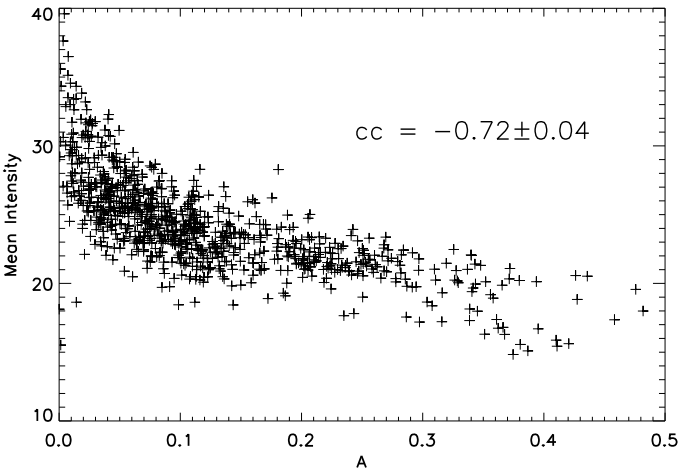

Figure 12 Scatter plot of mean intensity of CH pixels against fractional CH areas calculated from EIT 195 Å images.

derived in EIT 195 Å images with those obtained by SXI. We are using SXI level-2 files (SXI CH data product) and take for each day four SXI coronal images, provided around 1, 7, 13, and 19 UT. We apply our algorithm to the SXI images, with the only difference that for SXI images we use a fixed threshold of 0.15 DN instead of a varying one that was used

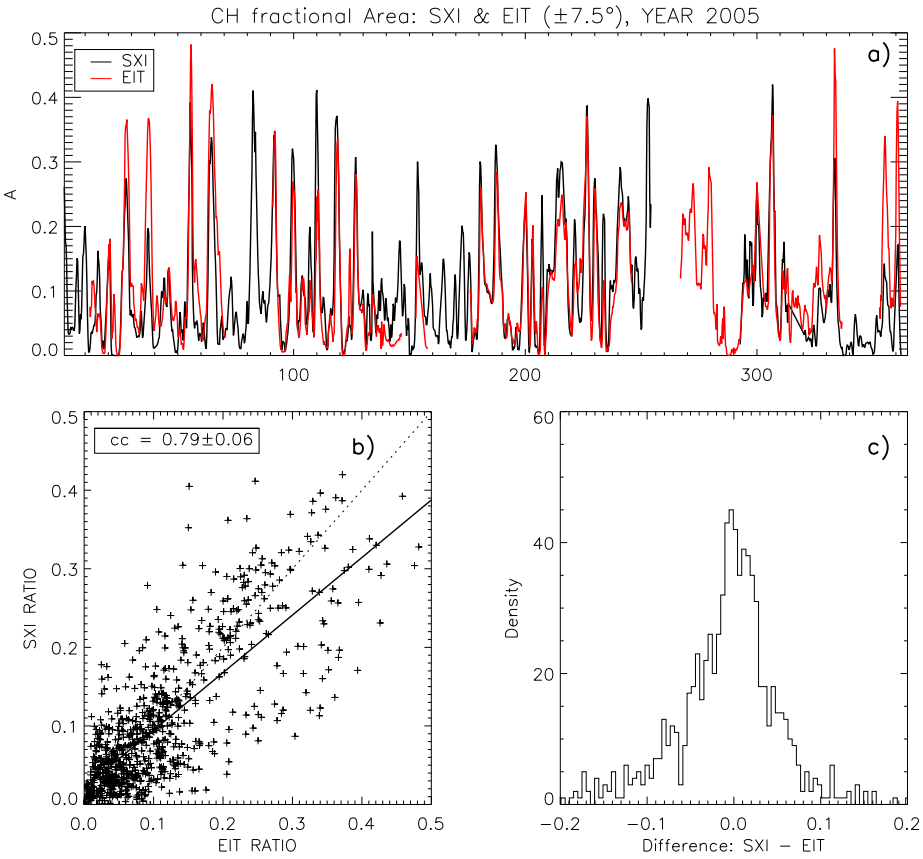

Figure 13 (a) CH fractional areas for the year 2005 obtained from SXI (black) and EIT (red). (b) Correlation between the SXI and EIT fractional CH areas A. The one-to-one correspondence is plotted as a dashed line and the regression fit as a straight line. (c) Histogram of the difference of the fractional CH areas obtained from EIT and SXI images.

on EIT images, delivering the same output but with a higher cadence of 6 h, as was used in Vršnak, Temmer, and Veronig (2007a).

The fractional CH areas for the year 2005 are plotted in Figure 13(a), where the black line indicates the CH areas obtained by SXI and the red line depicts the CH areas derived from EIT. Between 11 September and 20 October 2005, DOY 254 – 293, SXI entered a safe-hold mode causing a data gap. It is clearly visible that the shape and time of the occurring peaks are comparable, but the peak values may differ. Figure 13(b) shows a direct comparison of SXI and EIT fractional areas giving a correlation coefficient of 0.79 ± 0.06. The histogram of the differences of the CH areas derived from SXI and EIT is plotted in Figure 13(c). The mean of the distribution is -0.0061 ± 0.0036, *i.e.* there are no systematic differences in calculating CH areas from EIT and SXI images.

We also calculated the delays for certain solar wind parameters via cross-correlations in the time range of DOY 25 – 125 with a 6-h time resolution. The cross-correlation is calculated up to ± 20 days. The time lags derived for A–v, A–T, A–n, and A–B are 3.25, 2.75, 0.75, and 1.75 days. Similar to EIT we apply a linear function (for detailed information, see

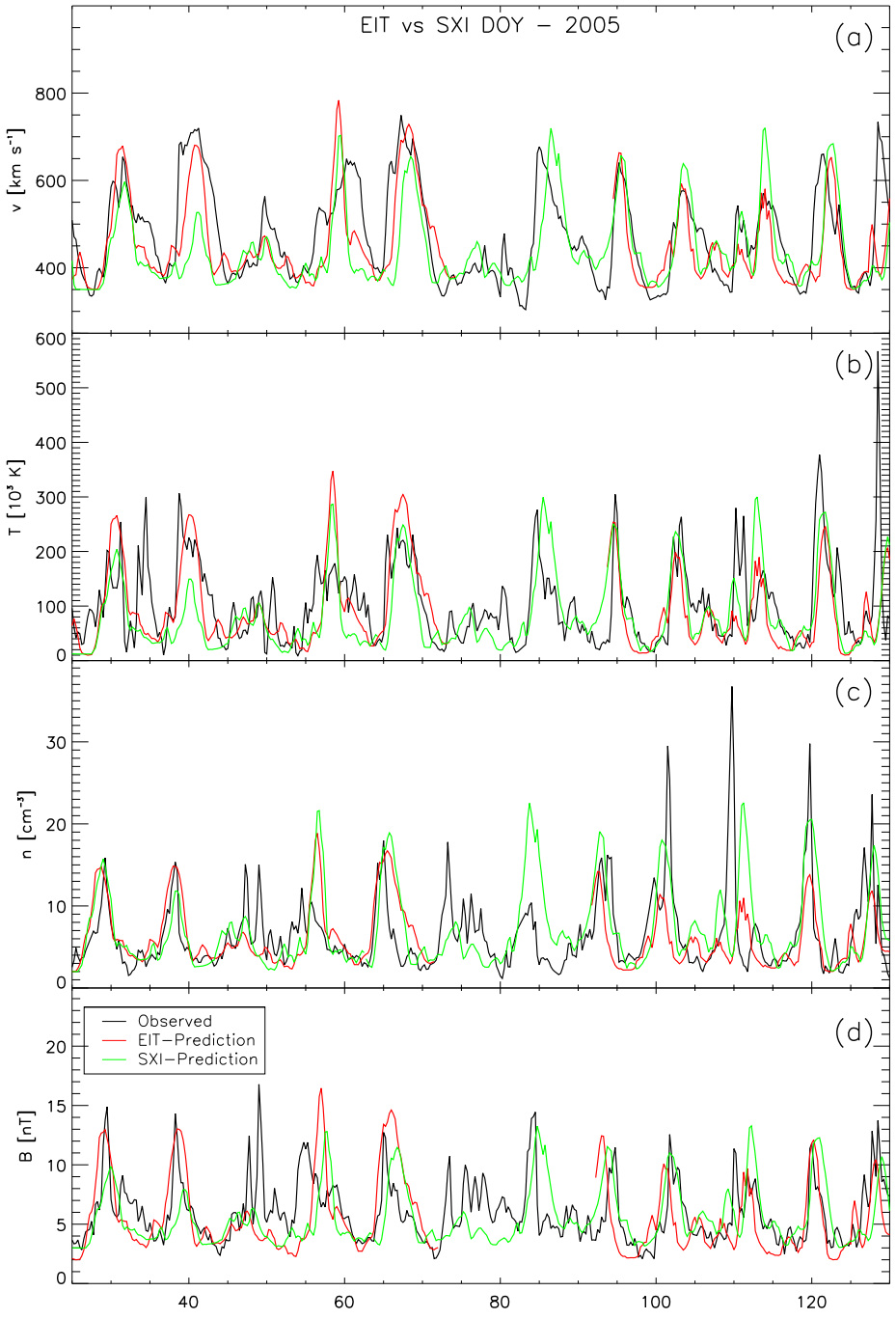

Figure 14 (a) Solar wind speed v, (b) proton temperature T, (c) proton density n, and (d) total magnetic field strength B for the time range of DOY 25 – 130, 2005. Shown are observations (black line), EIT predictions (red line), and SXI predictions (green line).

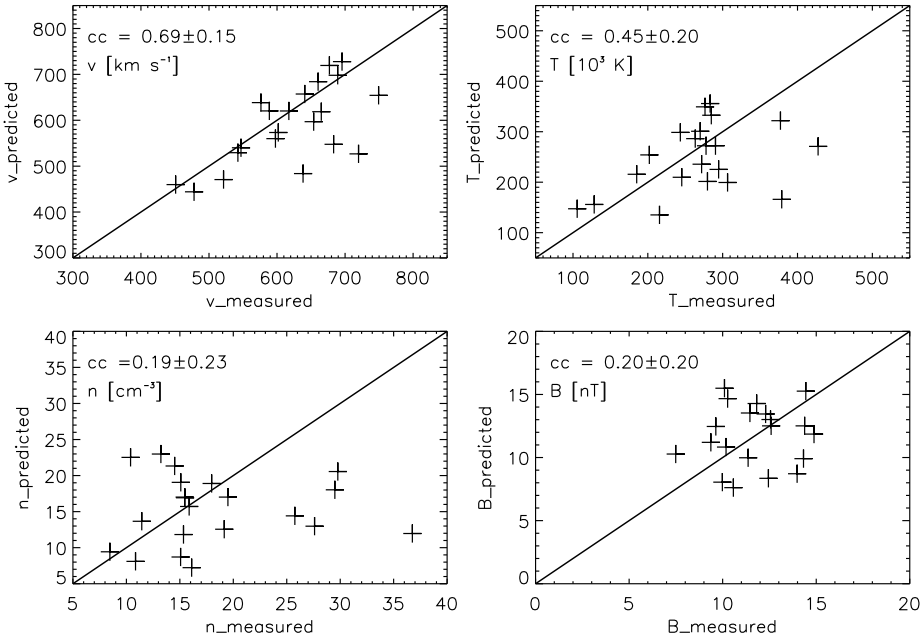

Figure 15 Same as Figure 7, but using SXI data.

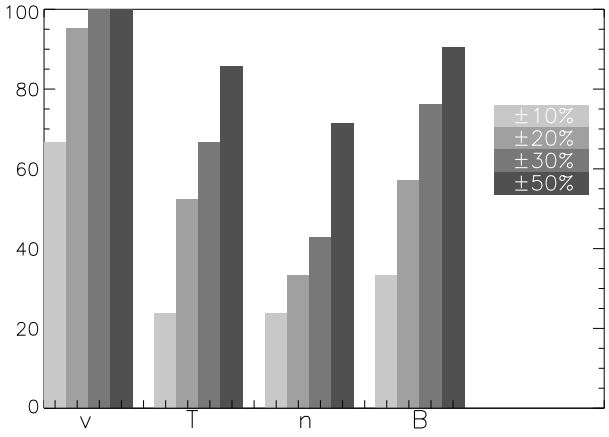

Figure 16 Probability in forecasting solar wind parameters via fractional CH areas provided by EIT 195 Å in a given percentage-based range around the measured peak values for solar wind speed v, temperature T, density n, and total magnetic fields strength B.

Vršnak, Temmer, and Veronig, 2007a) to the SXI A data and substitute the coefficients c_0 and c_1 for v, T, n, and B as follows: $c_0 = 350$, 12, 3, and 2; $c_1 = 900$, 700, 50, and 25.

Figure 15 shows a scatter plot of the 21 selected peaks in fractional areas A provided by SXI in comparison to measured solar wind parameters. A and v correlate with cc $= 0.69 \pm 0.15$ and A and T with cc $= 0.45 \pm 0.20$. No significant correlation is obtained for A–n (cc $= 0.19 \pm 0.23$) and A–B (cc $= 0.20 \pm 0.20$). In Figure 14 the EIT-prediction curve (red line) and the SXI-prediction curve (green line) are plotted together with the measurements (black line) for DOY 25 – 130, 2005.

5. Discussion and Conclusions

We have developed a fully automatic histogram-based algorithm for detecting CHs in SOHO/EIT 195 Å images in order to predict solar wind parameters (amplitude and arrival time) at 1 AU.

For the full year 2005, we selected a sample of 21 well-defined peaks in the CH fractional areas that relate to HSSs at 1 AU. The algorithm produces good forecasts for the solar wind speed peaks ($cc = 0.78 \pm 0.08$). It shows medium correlations for the proton temperature T with $cc = 0.41 \pm 0.22$ and the total magnetic field strength B with $cc = 0.41 \pm 0.16$. No significant correlation was found for the solar wind proton density n ($cc = 0.18 \pm 0.19$). Figure 16 displays the probability of predicting peak values in a certain percentage range of the measured peaks. In case of the solar wind speed, 95 % of all predicted v peaks lie in the range of ± 20 % of the measured values. The figure also shows that the prediction capability is worst for the proton density, where only 75 % of the predicted values lie within ± 50 % of the measured peak. This implies that the fractional CH area is no adequate indicator in predicting the solar wind density.

In most cases the algorithm predicts the peak times of solar wind parameters to within ± 0.5 days. In cases where no CMEs disturb the solar wind parameters, the algorithm can thus be used to deliver reliable forecasts of the solar wind speed up to 4 days ahead.

Weighting the fractional CH areas by the inverse mean intensity of the CH areas did not improve the forecast due to the fact that the size and the mean intensity are not independent parameters ($cc = -0.72 \pm 0.04$).

Our algorithm was also tested on GOES-12 SXI data in order to compare our outcome with the results of previous studies based on SXI observations. A correlation of $cc = 0.79 \pm 0.06$ was found for EIT and SXI fractional CH areas over the year 2005, and no systematic differences were obtained. The method developed thus provides a good means to relate CH areas observed on the Sun to the solar wind characteristics at 1 AU. In future studies, this method shall be applied to almost-real-time SDO/AIA images in order to present solar wind speed forecasts for the Earth environment up to 3 days in advance.

Acknowledgements Data supplied were courtesy of the SOHO/MDI and SOHO/EIT consortia. SOHO is a project of international cooperation between ESA and NASA. Full-disk X-ray images are supplied by courtesy of the Solar X-ray Imager (SXI) team. We thank the ACE SWEPAM and MAG instrument teams and the ACE Science Center for providing the ACE data. The research leading to these results has received funding from the European Commission's Seventh Framework Programme (FP7/2007 – 2013) under grant agreements No. 218816 (SOTERIA) and FP7 No. 263252 (COMESEP). M.T. gratefully acknowledges the Austrian Science Fund (FWF): FWF V195-N16.

References

Abramenko, V., Yurchyshyn, V., Watanabe, H.: 2009, Parameters of the magnetic flux inside coronal holes. *Solar Phys.* **260**, 43 – 57. doi:10.1007/s11207-009-9433-7.

Altschuler, M.D., Trotter, D.E., Orrall, F.Q.: 1972, Coronal holes. *Solar Phys.* **26**, 354 – 365. doi:10.1007/BF00165276.

Barra, V., Delouille, V., Kretzschmar, M., Hochedez, J.F.: 2009, Fast and robust segmentation of solar EUV images: algorithm and results for solar cycle 23. *Astron. Astrophys.* **505**, 361 – 371. doi:10.1051/0004-6361/200811416.

Cranmer, S.R. 2009, Coronal holes. *Living Rev. Solar Phys.* **6**(3). http://solarphysics.livingreviews.org/Articles/lrsp-2009-3/.

de Toma, G.: 2011, Evolution of coronal holes and implications for high-speed solar wind during the minimum between cycles 23 and 24. *Solar Phys.* **274**, 195 – 217. doi:10.1007/s11207-010-9677-2.

Del Zanna, G., Bromage, B.J.I.: 1999, The elephant's trunk: spectroscopic diagnostics applied to SOHO/CDS observations of the August 1996 equatorial coronal hole. *J. Geophys. Res.* **104**, 9753 – 9766. doi:10.1029/1998JA900067.

Delaboudinière, J.P., Artzner, G.E., Brunaud, J., Gabriel, A.H., Hochedez, J.F., Millier, F., Song, X.Y., Au, B., Dere, K.P., Howard, R.A., Kreplin, R., Michels, D.J., Moses, J.D., Defise, J.M., Jamar, C., Rochus, P., Chauvineau, J.P., Marioge, J.P., Catura, R.C., Lemen, J.R., Shing, L., Stern, R.A., Gurman, J.B., Neupert, W.M., Maucherat, A., Clette, F., Cugnon, P., van Dessel, E.L.: 1995, EIT: Extreme-Ultraviolet Imaging Telescope for the SOHO mission. *Solar Phys.* **162**, 291 – 312. doi:10.1007/BF00733432.

Delouille, V., Barra, V., Hochedez, J.: 2007, Segmentation of SoHO/EIT images using fuzzy clustering algorithms. In: AGU Fall Meeting, A1107.

Detman, T., Smith, Z., Dryer, M., Fry, C.D., Arge, C.N., Pizzo, V.: 2006, A hybrid heliospheric modeling system: background solar wind. *J. Geophys. Res.* **111**, A07102. doi:10.1029/2005JA011430.

Gosling, J.T.: 1996, Physical nature of the low-speed solar wind. In: Habbal, S.R. (ed.) *Robotic Exploration Close to the Sun: Scientific Basis*, *AIP Conf. Proc.* **385**, American Institute of Physics, Woodbury, 17 – 24.

Gosling, J.T., Pizzo, V.J.: 1999, Formation and evolution of corotating interaction regions and their three dimensional structure. *Space Sci. Rev.* **89**, 21 – 52. doi:10.1023/A:1005291711900.

Henney, C.J., Harvey, J.W.: 2005, Automated coronal hole detection using He 1083 nm spectroheliograms and photospheric magnetograms. In: Sankarasubramanian, K., Penn, M., Pevtsov, A. (eds.) *Large-Scale Structures and Their Role in Solar Activity*, *ASP Conf. Ser.* **346**, 261 – 268.

Hill, S.M., Pizzo, V.J., Balch, C.C., Biesecker, D.A., Bornmann, P., Hildner, E., Lewis, L.D., Grubb, R.N., Husler, M.P., Prendergast, K., Vickroy, J., Greer, S., Defoor, T., Wilkinson, D.C., Hooker, R., Mulligan, P., Chipman, E., Bysal, H., Douglas, J.P., Reynolds, R., Davis, J.M., Wallace, K.S., Russell, K., Freestone, K., Bagdigian, D., Page, T., Kerns, S., Hoffman, R., Cauffman, S.A., Davis, M.A., Studer, R., Berthiaume, F.E., Saha, T.T., Berthiume, G.D., Farthing, H., Zimmermann, F.: 2005, The NOAA GOES-12 Solar X-ray Imager (SXI) 1. Instrument, operations, and data. *Solar Phys.* **226**, 255 – 281. doi:10.1007/s11207-005-7416-x.

Hundhausen, A.J.: 1972, Composition and dynamics of the solar wind plasma. In: Dyer, E.R., Roederer, J.G., Hundhausen, A.J. (eds.) *The Interplanetary Medium: Part II of Solar-Terrestrial Physics*, D. Reidel, Dordrecht, 1 – 31.

Kirk, M.S., Pesnell, W.D., Young, C.A., Hess Webber, S.A.: 2009, Automated detection of EUV polar coronal holes during solar cycle 23. *Solar Phys.* **257**, 99 – 112. doi:10.1007/s11207-009-9369-y.

Krieger, A.S., Timothy, A.F., Roelof, E.C.: 1973, A coronal hole and its identification as the source of a high velocity solar wind stream. *Solar Phys.* **29**, 505 – 525. doi:10.1007/BF00150828.

Krista, L.D., Gallagher, P.T.: 2009, Automated coronal hole detection using local intensity thresholding techniques. *Solar Phys.* **256**, 87 – 100. doi:10.1007/s11207-009-9357-2.

Lemen, J.R., Title, A.M., Akin, D.J., Boerner, P.F., Chou, C., Drake, J.F., Duncan, D.W., Edwards, C.G., Friedlaender, F.M., Heyman, G.F., Hurlburt, N.E., Katz, N.L., Kushner, G.D., Levay, M., Lindgren, R.W., Mathur, D.P., McFeaters, E.L., Mitchell, S., Rehse, R.A., Schrijver, C.J., Springer, L.A., Stern, R.A., Tarbell, T.D., Wuelser, J.P., Wolfson, C.J., Yanari, C., Bookbinder, J.A., Cheimets, P.N., Caldwell, D., Deluca, E.E., Gates, R., Golub, L., Park, S., Podgorski, W.A., Bush, R.I., Scherrer, P.H., Gummin, M.A., Smith, P., Auker, G., Jerram, P., Pool, P., Soufli, R., Windt, D.L., Beardsley, S., Clapp, M., Lang, J., Waltham, N.: 2012, The Atmospheric Imaging Assembly (AIA) on the Solar Dynamics Observatory (SDO). *Solar Phys.* **275**, 17 – 40. doi:10.1007/s11207-011-9776-8.

Luo, B., Zhong, Q., Liu, S., Gong, J.: 2008, A new forecasting index for solar wind velocity based on EIT 284 Å observations. *Solar Phys.* **250**, 159 – 170. doi:10.1007/s11207-008-9198-4.

McComas, D.J., Bame, S.J., Barker, P.L., Delapp, D.M., Feldman, W.C., Gosling, J.T., Santiago, E., Skoug, R.M., Tokar, R.L., Riley, P., Phillips, J.L., Griffee, J.W.: 1998, An unusual coronal mass ejection: First Solar Wind Electron, Proton, Alpha Monitor (SWEPAM) results from the Advanced Composition Explorer. *Geophys. Res. Lett.* **25**, 4289 – 4292. doi:10.1029/1998GL900174.

Munro, R.H., Withbroe, G.L.: 1972, Properties of a coronal "hole" derived from extreme-ultraviolet observations. *Astrophys. J.* **176**, 511 – 520. doi:10.1086/151653.

Neupert, W.M., Pizzo, V.: 1974, Solar coronal holes as sources of recurrent geomagnetic disturbances. *J. Geophys. Res.* **79**, 3701 – 3709. doi:10.1029/JA079i025p03701.

Newkirk, J.G.: 1967, Structure of the solar corona. *Annu. Rev. Astron. Astrophys.* **5**, 213 – 262. doi:10.1146/annurev.aa.05.090167.001241.

Nolte, J.T., Krieger, A.S., Timothy, A.F., Gold, R.E., Roelof, G.E.C., Lazarus, A.J., Sullivan, J.D., McIntosh, P.S.: 1976, Coronal holes as sources of solar wind. *Solar Phys.* **46**, 303 – 322. doi:10.1007/BF00149859.

Obridko, V.N., Shelting, B.D., Livshits, I.M., Asgarov, A.B.: 2009, Contrast of coronal holes and parameters of associated solar wind streams. *Solar Phys.* **260**, 191 – 206. doi:10.1007/s11207-009-9435-5.

Odstrcil, D., Pizzo, V.J.: 2009, Numerical heliospheric simulations as assisting tool for interpretation of observations by STEREO Heliospheric Imagers. *Solar Phys.* **259**, 297 – 309. doi:10.1007/s11207-009-9449-z.

Pizzo, V.J., Hill, S.M., Balch, C.C., Biesecker, D.A., Bornmann, P., Hildner, E., Grubb, R.N., Chipman, E.G., Davis, J.M., Wallace, K.S., Russell, K., Cauffman, S.A., Saha, T.T., Berthiume, G.D.: 2005, The NOAA GOES-12 Solar X-ray Imager (SXI) 2. Performance. *Solar Phys.* **226**, 283 – 315. doi:10.1007/s11207-005-7417-9.

Reeves, E.M., Parkinson, W.H.: 1970, An atlas of extreme-ultraviolet spectroheliograms from OSO-IV. *Astrophys. J. Suppl.* **21**, 1 – 30. doi:10.1086/190217.

Robbins, S., Henney, C.J., Harvey, J.W.: 2006, Solar wind forecasting with coronal holes. *Solar Phys.* **233**, 265 – 276. doi:10.1007/s11207-006-0064-y.

Scholl, I.F., Habbal, S.R.: 2008, Automatic detection and classification of coronal holes and filaments based on EUV and magnetogram observations of the solar disk. *Solar Phys.* **248**, 425 – 439. doi:10.1007/s11207-007-9075-6.

Smith, C.W., L'Heureux, J., Ness, N.F., Acuña, M.H., Burlaga, L.F., Scheifele, J.: 1998, The ACE Magnetic Fields Experiment. *Space Sci. Rev.* **86**, 613 – 632. doi:10.1023/A:1005092216668.

Stone, E.C., Frandsen, A.M., Mewaldt, R.A., Christian, E.R., Margolies, D., Ormes, J.F., Snow, F.: 1998, The Advanced Composition Explorer. *Space Sci. Rev.* **86**, 1 – 22. doi:10.1023/A:1005082526237.

Temmer, M., Vršnak, B., Veronig, A.M.: 2007, Periodic appearance of coronal holes and the related variation of solar wind parameters. *Solar Phys.* **241**, 371 – 383. doi:10.1007/s11207-007-0336-1.

Tousey, R., Sandlin, G.D., Purcell, J.D.: 1968, On Some Aspects of XUV Spectroheliograms. In: Kiepenheuer, K.O. (ed.) *Structure and Development of Solar Active Regions*, *IAU Symp.* **35**, 411 – 419.

Tsurutani, B.T., Gonzalez, W.D., Gonzalez, A.L.C., Tang, F., Arballo, J.K., Okada, M.: 1995, Interplanetary origin of geomagnetic activity in the declining phase of the solar cycle. *J. Geophys. Res.* **100**, 21717 – 21734. doi:10.1029/95JA01476.

Vaiana, G.S.: 1976, The X-ray corona from SKYLAB. *Phil. Trans. Roy. Soc. London A* **281**, 365 – 374. doi:10.1098/rsta.1976.0034.

Verbanac, G., Vršnak, B., Veronig, A., Temmer, M.: 2011, Equatorial coronal holes, solar wind high-speed streams, and their geoeffectiveness. *Astron. Astrophys.* **526**, A20. doi:10.1051/0004-6361/201014617.

Veselovsky, I.S., Persiantsev, I.G., Ryazanov, A.Y., Shugai, Y.S.: 2006, One-parameter representation of the daily averaged solar-wind velocity. *Solar Syst. Res.* **40**, 427 – 431. doi:10.1134/S0038094606050078.

Vršnak, B., Temmer, M., Veronig, A.M.: 2007a, Coronal holes and solar wind high-speed streams: I. Forecasting the solar wind parameters. *Solar Phys.* **240**, 315 – 330. doi:10.1007/s11207-007-0285-8.

Vršnak, B., Temmer, M., Veronig, A.M.: 2007b, Coronal holes and solar wind high-speed streams: II. Forecasting the geomagnetic effects. *Solar Phys.* **240**, 331 – 346. doi:10.1007/s11207-007-0311-x.

Wall, J.V., Jenkins, C.R.: 2003, In: *Practical Statistics for Astronomers*, Cambridge University Press, Cambridge, 54 – 74.

Wilcox, J.M.: 1968, The interplanetary magnetic field. Solar origin and terrestrial effects. *Space Sci. Rev.* **8**, 258 – 328. doi:10.1007/BF00227565.